

Propulsion of Gold Nanoparticles with Surface Plasmon Polaritons: Evidence of Enhanced Optical Force from Near-Field Coupling between Gold Particle and Gold Film

Kai Wang, Ethan Schonbrun, and Kenneth B. Crozier*

*School of Engineering and Applied Sciences, Harvard University,
Cambridge, Massachusetts 02138*

Received March 25, 2009; Revised Manuscript Received May 12, 2009

ABSTRACT

We experimentally demonstrate the enhanced propulsion of gold nanoparticles by surface plasmon polaritons (SPPs). Three dimensional finite difference time domain (FDTD) simulations indicate considerably enhanced optical forces due to the field enhancement provided by SPPs and the near-field coupling between the gold particles and the film. This coupling is an important part of the enhanced propulsion phenomenon. Finally, the measured optical force is compared with that predicted by FDTD simulations and proven to be reasonable.

The optical manipulation of gold nanoparticles is gaining increasing attention due to their broad applications in nanomaterials and nanobiotechnology.¹ Gold nanoparticles are particularly useful in biophysics as handles because the chemical properties of gold allow for various types of custom functionalization. This motivates the development of methods for the controlled manipulation of gold nanoparticles through optical forces, as these could prove useful for biophysical investigations. Gold nanoparticles have the added advantage of high polarizability, making trapping at lower laser powers possible.

Optical tweezers have proven to be highly successful for trapping dielectric particles to study biological systems. However, the stable trapping of metallic nanoparticles has proven to be difficult.²⁻⁴ Because of the strong absorption of metallic particles, stronger gradient forces are needed to overcome scattering and absorption forces for stable three-dimensional (3D) trapping.^{3,5} Since scattering and absorption forces decrease faster than gradient force with particle diameter, small gold nanoparticles are more suitable for optical trapping. In 1994, Svoboda and Block demonstrated the optical trapping of 36 nm diameter gold beads with a 7-fold higher trap stiffness than similarly sized polystyrene beads.⁵ More recently, Hansen et al. expanded the range of sizes of gold nanoparticles that can be optically trapped by

employing a water immersion objective and slightly overfilling the back aperture of the objective.⁶ They experimentally demonstrated single beam optical trapping of gold nanoparticles with diameters ranging from 18 to 254 nm. The optical trapping of silver nanoparticles has also been experimentally demonstrated.⁷

Conventional optical tweezers trap particles using focal spots whose sizes are limited by diffraction to approximately half a wavelength. This limits the gradient force achievable for a given input laser power. In addition, the size of the trapping region may be considerably larger than the size of the nanoparticle to be trapped. This motivated the proposal of optical trapping using surface plasmon resonance structures due to their ability to generate enhanced optical fields confined to subwavelength dimensions.⁸⁻¹² Using surface plasmon polaritons (SPPs) on a gold film, Garces-Chavez et al. observed the self-organization of dielectric particles over a large area through optical and thermal convection forces.¹³ Volpe et al. employed a photonic force microscope to measure the enhancement of optical forces on dielectric particles by SPPs. The particles were 500 nm above the gold film and thus did not disturb the SPPs excessively.¹⁴ Since gold nanoparticles have high polarizability and are able to support surface plasmon resonance, they should have stronger interaction with metallic surface plasmon resonant trapping structures. In this letter, distinct from previous work we observe the enhanced manipulation of gold nanoparticles above a gold film by measuring the velocity of gold particles

* To whom correspondence should be addressed. E-mail: kcrozier@seas.harvard.edu. Telephone: 617-496-1441. Fax: 617-495-2489. Address: Maxwell Dworkin 147, Harvard University, 33 Oxford Street, Cambridge, MA 02138.

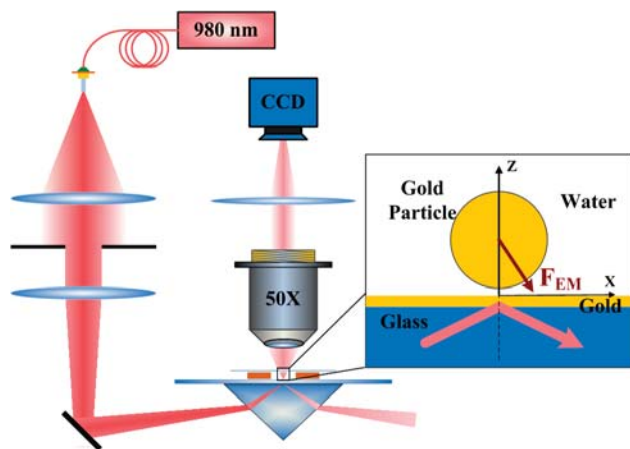


Figure 1. Experimental setup.

pushed by optical radiation forces arising from SPP excitation. Since the gold particles are very close to the gold film, the resultant near-field coupling greatly enhances the field intensity between them. In this way, the optical near field force occurring in the case of two gold structures with a small gap between them can be studied. The work presented here is quite different from previous studies on the propulsion of gold particles by the evanescent field above a dielectric surface,^{15–17} since those investigations did not involve the coupling phenomenon, nor the use of surface plasmon polaritons on a flat metal film. Also, our system is highly effective at transferring momentum from photons to gold nanoparticles. For example, consider the results reported by S. Gaugiran et al., where a high power density was needed in a silicon nitride waveguide to propel gold nanoparticles.¹⁸ By contrast, the use of SPPs in our system results in comparable propulsion velocities being achieved at much lower illumination intensities and over a larger area.

Experiments are performed using a Kretschmann prism-coupling geometry. The setup is shown in Figure 1. The laser source is a pigtailed semiconductor diode laser (980 nm) with a polarization-maintaining optical fiber output. The beam is expanded and spatially filtered by an iris to control the beam diameter. The resulting beam of ~ 6 mm in diameter is then loosely focused by a 20 cm focal length lens and directed into a prism ($n = 1.51$) after being reflected by a mirror. The mirror sits on a rotation stage and thus can be used to control the incident angle accurately over a wide range. The resulting $1/e^2$ intensity focused spot has an elliptical shape of $\sim 40 \mu\text{m} \times 80 \mu\text{m}$ on the surface of the sample, which is estimated by Gaussian beam theory. A sample chamber containing gold colloids in water is placed on top of the prism with immersion oil in between. The chamber consists of a glass microscope slide, an SU8 spacer, and a glass cover slide on top. The SU8 spacer is fabricated on the glass cover slide and is $\sim 5 \mu\text{m}$ thick. The use of a thin spacer layer minimizes thermal convection caused by heating of the gold film by laser illumination.¹³ Before the glass cover slide is stuck on to the glass microscope slide, gold and SiO_2 films are deposited on the glass slide. The gold film, 55 nm thick, is formed by thermal evaporation. The SiO_2 film, 5 nm thick, is formed by atomic layer deposition with the goal of

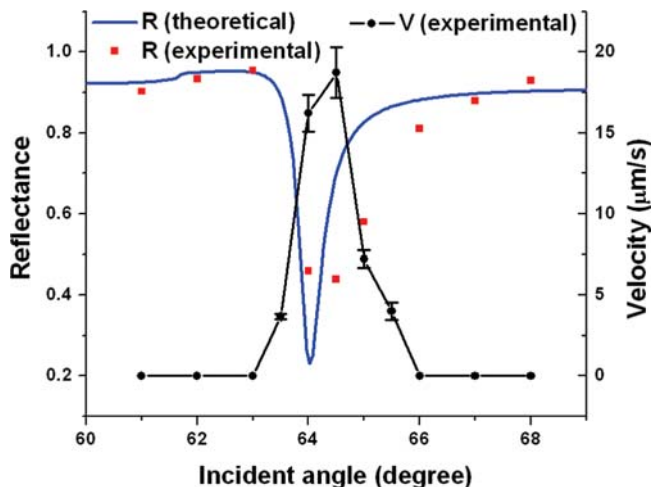


Figure 2. Experimentally measured reflectance (red squares) and particle velocity (black dots) as a function of incident angle. For the velocity measurements, illumination intensity is $6 \times 10^6 \text{ W/m}^2$. Theoretically calculated reflectance is shown as the blue curve.

preventing adhesion between the gold nanoparticles and the gold film. We put the gold colloid solution directly into chamber without dilution after receiving it from the supplier (Ted Pella Corp.). The gold colloids are 250 nm diameter spheres with a reported standard deviation ± 20 nm. The concentration of the gold colloids is $3.6 \times 10^8/\text{ml}$. A microscope objective (50 \times , Nikon CFI 60 LU Plan Epi ELWD infinity-corrected, $\text{NA} = 0.55$) is used to collect the light scattered by the gold particles in the evanescent field and to form an image on the charge coupled device (CCD) camera (ImagingSource DMK 21F04).

In order to couple the power into the SPP efficiently, it is desirable to decrease the divergence of the beam as much as possible. On the other hand, this decreases the intensity of the focused spot. Balancing these considerations, we choose the divergence of the beam incident on the prism to be 0.8 degrees. This is achieved by focusing a 6 mm diameter beam with a lens having a focal length of 20 cm. This allows us to achieve a sharp peak of the SPP resonance and a reasonable intensity simultaneously.

To confirm the excitation of SPPs, the reflectance of the glass/gold/ SiO_2 /water stack is measured. The input beam is transverse magnetic (TM) polarized. The experimental results (Figure 2) show that power is coupled to SPP effectively when the incident angle is around 64° , as evidenced by the reflectance dip. The measured data points are in reasonable agreement with theoretical calculations that take the dielectric constant of gold at $\lambda_0 = 980 \text{ nm}$ as $-44.4141 + 3.3065i$.¹⁹ The experimentally measured reflectivity dip is a little wider than theory predicts, but this can be expected because of the divergence of the incident beam. By tracking the positions of gold nanoparticles using the CCD camera images, we are able to determine particle velocity. Observations are made over an area approximately corresponding to the $1/e^2$ intensity region of the illumination beam. The trajectory of a nanoparticle in this evanescent field observation region is governed by a combination of propulsion from SPPs and Brownian motion. The average velocity of a nanoparticle

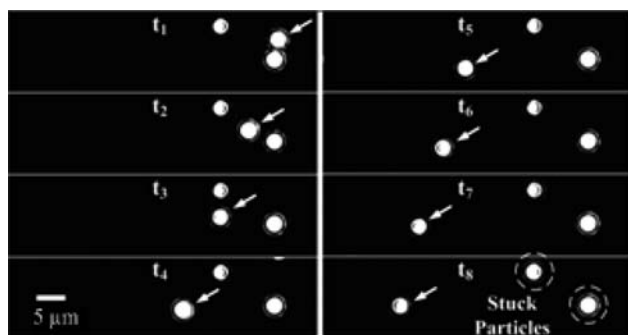


Figure 3. Time sequence of scattered light images of gold nanoparticles, as recorded by CCD camera. The images have dimensions of $70 \mu\text{m} \times 20 \mu\text{m}$, and the time interval between images is $1/6 \text{ s}$. The gold nanoparticle denoted by the arrow moves right to left. Two nanoparticles, indicated by dashed circles, are stuck to the sample surface.

while in the observation region is found using $\bar{v} = [x(t_0 + t_{\text{stay}}) - x(t_0)]/t_{\text{stay}}$. Here, t_0 is the time at which the nanoparticle enters the evanescent field of the observation region, and t_{stay} is the period for which it stays in this region. The average velocity varies between particles due to the variation in intensity and hence scattering force across the beam, randomness in the positions at which particles enter the evanescent field, and Brownian motion. However, by making observations of \bar{v} of different particles, an average velocity in the observation region can be found. In Figure 2, we plot \bar{v} , averaged over multiple particles, as a function of incident angle (black dots) for a fixed illumination field intensity of $6 \times 10^6 \text{ W/m}^2$ incident on the gold film. This is the average illumination intensity over the $1/e^2$ area of the beam. From Figure 2, it can be seen that particle velocity peaks when SPPs are excited. The error bars indicate the standard deviation of \bar{v} , obtained by measurements on different particles. When the incident angle is away from the SPP angle, or there is no gold film on the glass, Brownian motion dominates. For this case, we observe that the particles do not remain in the evanescent field for sufficient time for a velocity measurement to be taken. The velocity in that case should be very small, if not zero, and far smaller than that achieved when SPPs are excited. The same experiment is also carried out when the incident beam is transverse electric (TE) polarized. For this case, no propulsion effect is observed. A typical sequence of scattered light images of particles recorded by the CCD camera at a rate of 30 frames per second (fps) is shown in Figure 3. One of the particles, indicated by an arrow, moves across the image field from right to left in successive frames. The other two particles, circled with dashed lines, are stuck on the surface, and do not move.

In addition to particle tracking, the CCD camera images allow the brightness of the light scattered by a particle to be determined as a function of time. Here, we define the coordinate axes so that the sample plane is the x - y plane. The $+z$ axis is therefore normal to the gold film and directed into the water. The plane of incidence of the laser illumination is the x - z plane. The excited SPPs are therefore confined in the z direction and propagate in the x direction. Gold

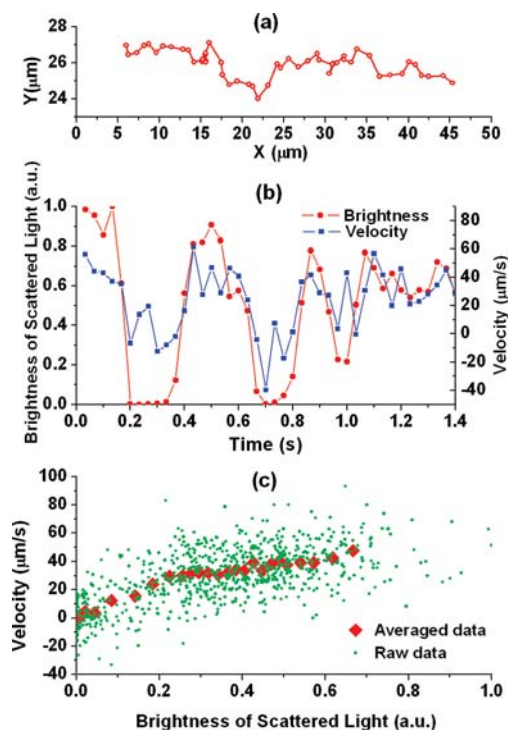


Figure 4. (a) Typical trajectory of a gold particle driven by SPPs. Time between data points is $1/30 \text{ s}$. Particle moves from right to left. (b) Instantaneous brightness and velocity of a particle driven by SPPs. (c) Particle velocity and brightness scatter plot. Raw data (green dots) are collected from a number of particles over a period of time. Averaged data (red symbols) are obtained by averaging brightness and velocity of 30 neighboring raw data points.

nanoparticles experience random thermal forces in all three dimensions, the optical scattering force in the x direction and the optical gradient force in the $-z$ direction. A typical trajectory of a particle in x - y plane is shown in Figure 4a and is obtained by frame-by-frame image analysis of the CCD images. Since there is no optical force in the y direction, the motion of the gold nanoparticles in this direction is purely due to Brownian motion. As described later, observation of the particle motion in this direction provides useful information on the fluid viscosity. Because of the exponential decay characteristic of the evanescent field, the brightness of the light scattered by the gold particles allows us to monitor their positions in the z direction, which vary due to Brownian motion. The variance of the particles' position in the z direction will modify the optical force in the x direction. Together with Brownian motion in the x direction, this results in the particle velocity in the x direction being nonconstant. From the trajectory of the particle, averaged particle's velocity between two continuous frames can be simply calculated by $v(t_0 + (1/2)\Delta t) = [x(t_0 + \Delta t) - x(t_0)]/\Delta t$. The brightness at the same instant in time is estimated by $P(t_0 + (1/2)\Delta t) = [P(t_0 + \Delta t) + P(t_0)]/2$, where $P(t_0)$ is the brightness at time t_0 , found from the CCD camera images. The result is shown in Figure 4b and shows a strong correlation between velocity and brightness. This can be seen more clearly by plotting velocity as a function of brightness using data collected from many particles. Because of the Brownian motion, the relationship between brightness and

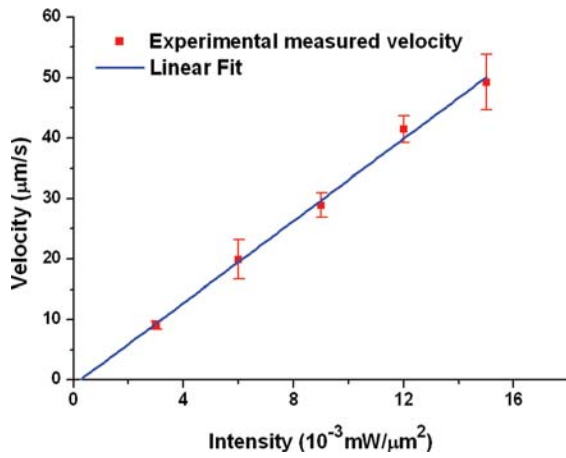


Figure 5. Experimentally measured particle velocity as a function of illumination intensity. The incident angle is 64.5° .

velocity cannot be seen clearly by examination of the raw experimental data (green dots), as shown in Figure 4c. However, this noise can be reduced by performing a running average over neighboring points. Each averaged data point of Figure 4c (red symbols) is obtained by averaging the brightnesses and velocities of 30 neighboring raw data points. The averaged data shows that velocity increases with the brightness of scattered light. The correlation between brightness and velocity is clear evidence that the observed propulsion is due to optical forces. The optical force is proportional to the total momentum change of the scattered photons. We would therefore expect that brighter particles, which scatter more light, would move at higher velocities, which is the case. On the other hand, if the particles were being pushed by thermal convection flow accompanying SPP excitation, we would not expect an appreciable variation in particle velocity over the evanescent field decay length. We would therefore not expect to see the strong correlation between velocity and brightness that we observe in Figure 4c. As an additional check, we carry out the same experiment with 150 nm diameter gold particles. These smaller particles experience much weaker optical forces and therefore provide means for determining whether particle movement might be due to water flow in the chamber arising from heating. No particle drift is observed, indicating a thermal convection-free environment.

In addition to measuring particle velocity as a function of incident angle, we measure it as a function of illumination intensity. Results are shown in Figure 5 and are obtained for a fixed incident angle of 64.5° . Experimental results show that velocity is almost linearly proportional to input power and can reach as high as $\sim 50 \mu\text{m/s}$ without the presence of thermal convection.

To gain insight into this phenomenon, we employ 3D FDTD (RSoft 8.01) calculations and use the Maxwell stress tensor method to calculate the optical force F_{EM} with simulation parameters chosen to match those of the experiments. As shown in Figure 6, the gold particle has a diameter of 250 nm, and the gold film is 55 nm thick. The gap between the gold particle and film is chosen to be 10 nm, equal to the Debye length estimated for the experimental parameters

used. The electrostatic force between the negatively charged gold particle and the negatively surface-charged SiO_2 film is believed to be the main mechanism that prevents the gold particle from sticking to the surface.²⁰ The gold particle solution has a pH of ~ 9 and gold particles are negatively surface charged to avoid aggregation. The estimated concentration of ions in the solution is $\sim 10^{-4} \text{ mol/L}$. The Debye length is therefore $\sim 10 \text{ nm}$. While we do not know the precise separation between the gold nanoparticle and film, for the calculations we assume it to be the Debye length, as this is the characteristic length of the electrostatic interaction. To model the particle, gap, and film accurately, we use a nonuniform simulation grid, ranging from 2 nm near material interfaces to 10 nm further from these boundaries. Quasi continuous wave (CW) illumination is used, and the field components are sampled after the simulation reaches steady state. As a check, we find the optical force by integrating the Maxwell stress tensor over different surfaces enclosing the particle and for different simulation times. These simulations verify that the calculated optical force is stable. Calculations are performed both for the SPP case and the total internal reflection (TIR) case in which the sample consists of a glass substrate with no gold film. The typical power flow distributions, given by the magnitude of the time-averaged Poynting vector, $\mathbf{S} = (\text{Re}[\mathbf{S}_x]^2 + \text{Re}[\mathbf{S}_y]^2 + \text{Re}[\mathbf{S}_z]^2)^{1/2} = (\text{Re}[\mathbf{S}_x]^2 + \text{Re}[\mathbf{S}_z]^2)^{1/2}$ calculated for the TIR and SPP cases are shown in Figure 6. The figure shows that the power flow magnitudes are much higher in the SPP case than the TIR case, which is due to the intense fields resulting from SPP excitation. Also, in the SPP case the gold particle disturbs the EM field much more strongly than it in the TIR case. The calculated optical force as a function of incident angle is shown in Figure 7. The angle of the force (defined in Figure 6) is also shown in Figure 7. At the SPP angle, the optical force is ~ 22 times larger for the SPP case than the TIR case. This is larger than what would be predicted just from the enhancement in intensity of the SPP case by comparison to the TIR case, $|E_{SPP}/E_{TIR}|^2$, which is ~ 10 times. Interestingly, the simulation results also indicate that for the SPP case the optical force is directed much more toward the sample than for the TIR case. This is true even if the incident illumination is far from the SPP excitation angle. This feature is purely due to the interaction between gold film and gold particle. In Figure 8, we plot the optical force on the gold particle as a function of gap size. The attractive force F_z that pulls the particle down to the surface decreases sharply with increasing gap size. It is due to the near field interaction between gold film and gold particle. If we approximate the gold particle as a dipole near the gold film, it will induce an image dipole in the gold film. In the static approximation, the ratio between the induced dipole moment and the dipole moment of the gold nanoparticle is $(\epsilon - \epsilon_{\text{water}})/(\epsilon + \epsilon_{\text{water}})$, where ϵ and ϵ_{water} are the relative permittivities of gold and water, respectively. At the operating wavelength of 980 nm, the permittivity of gold is large, so the ratio of dipole moments is approximately unity. Thus, the interaction between gold particle and gold film can be understood by analyzing the interaction between two gold particles separated

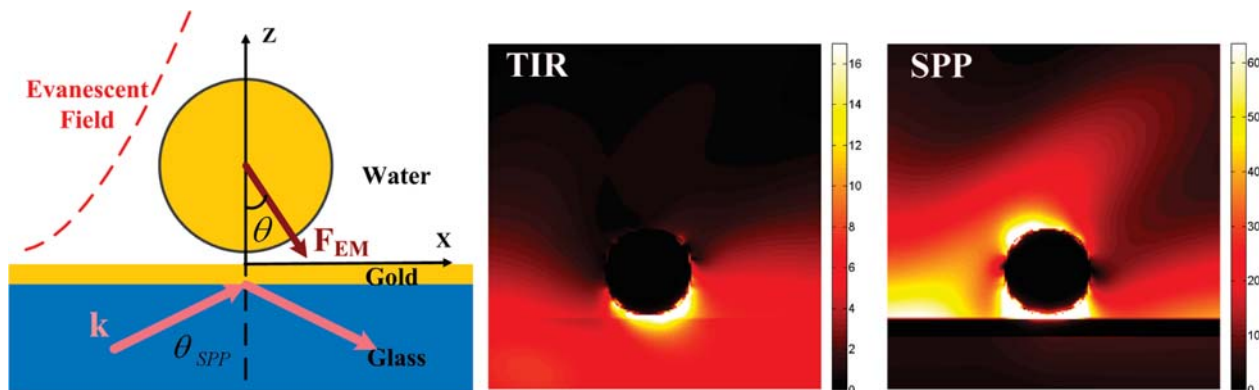


Figure 6. Left: Schematic of optical manipulation of gold nanoparticle using SPPs. Middle and right: 3D FDTD calculated power flow distributions at $y = 0$ cross-section for TIR and SPP cases. There is no gold film on the glass substrate for the TIR case. For the SPP case, there is a gold film, 55 nm thick, on the glass substrate.

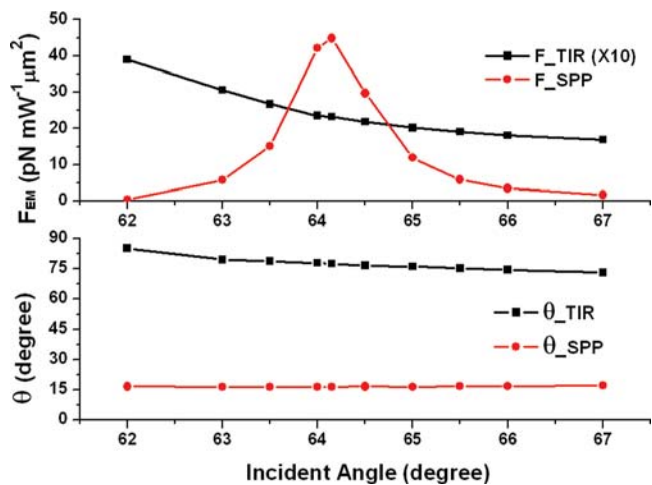


Figure 7. Optical forces and their directions as a function of incident angles, as found by 3D FDTD simulations. Optical force is normalized to incident intensity.

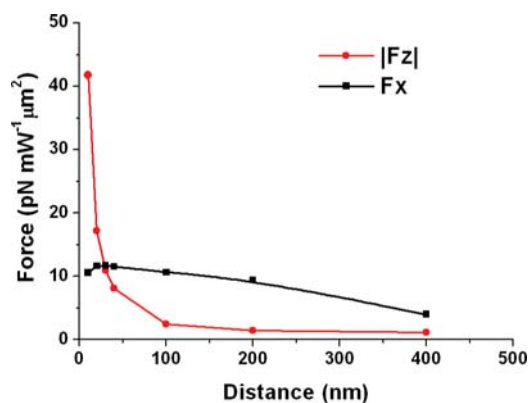


Figure 8. Optical forces as a function of particle-film gap, found from 3D FDTD simulations.

by a small gap. The optical force between two coupled gold nanoparticles illuminated by a plane wave has been studied numerically, and results show complex behaviors depending on the wavelength, the polarization of the electromagnetic field, the size of the particles, and the size of the gap.^{21–24} These previous studies predict a strong attractive force when the electric field is across the gap and gold particles are far away from resonance. This is the case of our experiment, as

250 nm diameter gold particles resonate at about $1.3 \mu\text{m}$. The strong attractive force decays rapidly with increasing gap size. This is very similar to the behavior of F_z shown in Figure 8. Intuitively, the attractive optical force comes from the interaction between two dipoles which are in phase when the gap is small. This force increases greatly when the two particles come close to each other because of large field enhancement in the gap. At the same time, the FDTD simulations predict that, as the particle approaches the gold film, the optical force F_x increases first and then decreases a little. The initial increase of F_x is due to the increased field intensity in the evanescent field. The decrease of F_x when the gold particle is very close to the surface is not well understood here and will be the topic of future investigations.

From the measured velocity, the optical force F_x can be calculated if we know the drag coefficient μ of the particle in the solution, as these are related by $F_x = v\mu$, where v is the velocity. When the particle is far from the surface, the drag coefficient is given by $\mu = 6\pi\eta a$, where η is the dynamic viscosity and a is the radius of the particle, assumed to be spherical. For a 250 nm diameter sphere in water at room temperature, we have $6\pi\eta a = 2.4 \times 10^{-9} \text{ (N}\cdot\text{s/m)}$. However, to describe our experimental results accurately, we need to take temperature variation into account. The temperature could be higher than the room temperature because the gold film absorbs a large portion of the input laser power when the SPP is excited. The dynamic viscosity of water is very sensitive to the temperature and thus can significantly affect the measured optical force. However, the temperature can be estimated by analyzing the particles' Brownian motion. Since particles experience no optical force in the y direction, the diffusion coefficient measured in this direction $D = \langle \Delta y^2 \rangle / (2\Delta t)$ can be used to estimate the temperature of the water by the Einstein relationship $D = (k_B T_{est}) / \mu = (k_B T_{est}) / (6\pi a \eta(T_{est}))$, where $\eta(T)$ is known as a function of temperature.²⁵ As shown in Figure 9, the incident angle is fixed at 64.5° and the measured diffusion coefficient (red symbols) increases monotonically with input power because the temperature increases due to ohmic losses in the gold film. This then allows optical force F_x to be found from F_x

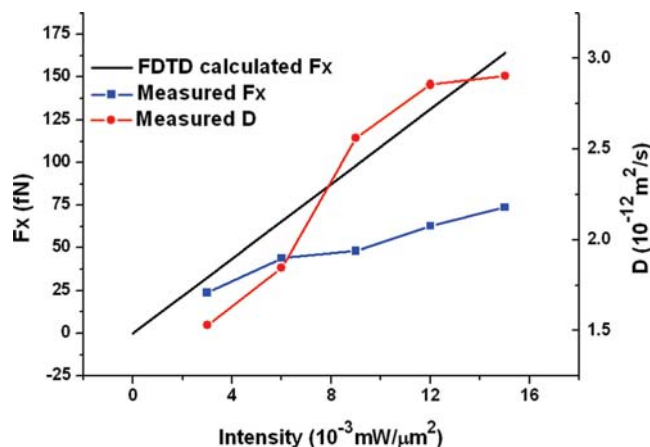


Figure 9. Experimentally measured diffusion coefficient D , measured optical force F_x , and FDTD calculated optical force F_x as a function of incident intensity. Incident angle is fixed at 64.5° . Gold particles have diameters of 250 nm.

$= (k_B T_{\text{est}} \nu) / D$, as shown by the blue symbols of Figure 9. It can be seen that the experimental results for F_x are in reasonable agreement with the predictions of the FDTD calculations. The FDTD calculations employ plane wave illumination with intensity matching the illumination intensity of the experiments, averaged across the $1/e^2$ diameter of the beam. Possible explanations for the differences between theory and experiment are discussed below.

First, the nonzero divergence of the input beam decreases the coupling efficiency of the input beam to the SPPs. In the FDTD simulations, the incoming beam is a plane wave. The coupling efficiency γ in this case can be determined from the reflectance R , $\gamma = 1 - R = 0.77$. For the experiments, the actual coupling efficiency γ_{act} can be estimated from the measured reflectance shown in Figure 2 to be $\gamma_{\text{act}} = 0.56$. Because the coupling efficiency of the experiments is smaller than that used for the theoretical calculations of the optical force, the illumination intensity is overestimated in these calculations. This results in the theoretical calculations overestimating the optical force. If we were to repeat the theoretical calculations using an effective intensity $I_{\text{eff}} = I(\gamma/\gamma_{\text{act}}) = 1.37 \times I$, these calculations should show better agreement with the experiments.

Second, an important factor that has to be taken into consideration is the effect of the surface on particles' dynamics when particle is very close to it. According to Faxen's law, the effective drag coefficient experienced by a particle will have an enhancement factor β ($\mu_{\text{eff}} = \mu\beta$, $\beta \geq 1$) when it gets closer to a surface.² The enhancement factor β depends on the particle's size and the distance between the particle and the surface. It will affect the measured optical force (blue line in Figure 9) in two ways. First, the temperature T_{est} determined above is likely to be an underestimate of the actual temperature T_{act} . This is because when Faxen's law is taken into account, the Einstein relationship is modified to be $D = (k_B T_{\text{act}}) / \mu_{\text{eff}} = (k_B T_{\text{act}}) / (6\pi\eta(T_{\text{act}})\beta)$. When Faxen's law is not taken into account, therefore, the optical force F_x^{est} is therefore underestimated as $F_x^{\text{est}} = (k_B T_{\text{est}} \nu) / D < F_x^{\text{act}} = (k_B T_{\text{act}} \nu) / D$. Second, it is entirely

possible that the enhancement factor β increases with intensity because the stronger optical force leads to a decrease in the average particle-surface distance. This would result in a larger discrepancy between the measured and predicted optical force at higher input power levels.

In conclusion, we experimentally observed the enhanced propulsion of gold nanoparticles by SPPs. From 3D FDTD simulations, we attribute the enhanced optical force to field enhancement due to SPP excitation and near-field coupling between the gold nanoparticles and the gold film. Because of the field enhancement due to SPP excitation, 250 nm diameter gold particles can be propelled at illumination field intensities as low as $3 \times 10^6 \text{ W}/\text{m}^2$ at which the optical force is $\sim 25 \text{ fN}$. The near-field coupling between the gold nanoparticles and the gold film provides a strong attractive force that keeps the gold nanoparticles in the evanescent field region of the SPP. The optical force is experimentally estimated by measuring the average velocity and by characterizing the Brownian motion of the gold nanoparticles to find the drag coefficient. The experimentally determined optical forces are in good agreement with FDTD calculation at low input power levels, with some deviation at higher input power levels. This work provides a promising way to manipulate metallic particles over a large area at reasonable input power levels. Additionally, we anticipate that our letter may motivate the use of the metallic particle-film system as an alternative means for understanding the optical forces between optically coupled metallic particles.

Acknowledgment. This work was supported by the Defense Advanced Research Project Agency (DARPA) and by the National Science Foundation (NSF). Fabrication work was carried out in the Harvard Center for Nanoscale Systems, which is supported by the NSF.

References

- (1) Daniel, M. C.; Astruc, D. *Chem. Rev.* **2004**, *104*, 293.
- (2) Neuman, K. C.; Block, S. M. *Rev. Sci. Instrum.* **2004**, *75*, 2787.
- (3) Ashkin, A. *Science* **1980**, *210*, 1081.
- (4) Sasaki, K.; Koshioka, M.; Misawa, H.; Kitamura, N.; Masuhara, H. *Appl. Phys. Lett.* **1992**, *60*, 807.
- (5) Svoboda, K.; Block, S. M. *Opt. Lett.* **1994**, *19*, 930.
- (6) Hansen, P. M.; Bhatia, V. K.; Harrit, N.; Oddershede, L. *Nano Lett.* **2005**, *5*, 1937.
- (7) Bosanac, L.; Aabo, T.; Bendix, P. M.; Oddershede, L. B. *Nano Lett.* **2008**, *8*, 1486.
- (8) Novotny, L.; Bian, R. X.; Xie, X. S. *Phys. Rev. Lett.* **1997**, *79*, 645.
- (9) Quidant, R.; Petrov, D.; Badenes, G. *Opt. Lett.* **2005**, *30*, 1009.
- (10) Righini, M.; Volpe, G.; Girard, C.; Petrov, D.; Quidant, R. *Phys. Rev. Lett.* **2008**, *100*, 186804.
- (11) Grigorenko, A. N.; Roberts, N. W.; Dickinson, M. R.; Zhang, Y. *Nat. Photonics* **2008**, *2*, 365.
- (12) Righini, M.; Ghenuche, P.; Cherukulappurath, S.; Myroshnychenko, V.; Garcia de Abajo, F. J.; Quidant, R. *Nano Lett.* [Online early access]. DOI:10.1021/nl803677x.
- (13) Garces-Chavez, V.; Quidant, R.; Reece, P. J.; Badenes, G.; Torner, L.; Dholakia, K. *Phys. Rev. B* **2006**, *73*, 085417.
- (14) Volpe, G.; Quidant, R.; Badenes, G.; Petrov, D. *Phys. Rev. Lett.* **2006**, *96*, 238101.
- (15) Ng, L. N.; Zervas, M. N.; Wilkinson, J. S. *Appl. Phys. Lett.* **2000**, *76*, 1993.
- (16) Sasaki, K.; Hotta, J. *Opt. Lett.* **2000**, *25*, 1385.
- (17) Yang, A. H. J.; Lersuchatawanich, T.; Erickson, D. *Nano Lett.* **2009**, *9*, 1182.
- (18) Gaugiran, S.; Getin, S.; Fedeli, J. M.; Derouard, J. *Opt. Express* **2007**, *15* (13), 8146–8156.

- (19) Palik, E. D. *Handbook of optical constants of solids II*; Academic Press: Boston, 1991.
- (20) Behrens, S. H.; Grier, D. G. *J. Chem. Phys.* **2001**, *115*, 6716.
- (21) Zelenina, A. S.; Quidant, R.; Nieto-Vesperinas, M. *Opt. Lett.* **2007**, *32*, 1156.
- (22) Novotny, L.; Henkel, C. *Opt. Lett.* **2008**, *33*, 1029.
- (23) Sepulveda, B.; Alegret, J.; Kall, M. *Opt. Express* **2007**, *15*, 14914.
- (24) Gaugiran, S.; Getin, S.; Fedeli, J. M.; Derouard, J. *Opt. Express* **2007**, *15*, 8146.
- (25) Watson, J. R.; Basu, R. S.; Sengers, J. V. *J. Phys. Chem. Ref. Data* **1980**, *9*, 1255.

NL900944Y